J. Fluid Mech. (2009), *vol.* 626, *pp.* 241–262.
doi:10.1017/S002211200900576X Printed in the United Kingdom

Evolution of flat-plate wakes in sink flow

MEHRAN PARSHEH[1] AND ANDERS A. DAHLKILD[2]†

[1]St. Anthony Falls Laboratory, University of Minnesota, Minneapolis, MN 55414, USA

[2]Department of Mechanics, Royal Institute of Technology, KTH, SE-100 44 Stockholm, Sweden

(Received 12 March 2008 and in revised form 22 December 2008)

Evolution of flat-plate wakes in sink flow has been studied both analytically and experimentally. For such wakes, a similarity solution is derived which considers simultaneous presence of both laminar and turbulent stresses inside the wake. This solution utilizes an additional Reynolds-stress term which represents the fluctuations similar to those in wall-bounded flows, accounting for the fluctuations originating from the plate boundary layer. In this solution, it is shown that the total stress, the sum of laminar and Reynolds shear stresses, becomes self-similar. To investigate the accuracy of the analytical results, the wake of a flat plate located at the centreline of a planar contraction is studied using hot-wire anemometry. Wakes of both tapered and blunt edges are considered. The length of the plates and the flow acceleration number $K = 6.25 \times 10^{-6}$ are chosen such that the boundary-layer profiles at the plate edge approach the self-similar laminar solution of Pohlhausen (*Z. Angew. Math. Mech.*, vol. 1, 1921, p. 252). A short plate in which the boundary layer at the edge does not fully relaminarize is also considered. The development of the turbulent diffusivity used in the analysis is determined empirically for each experimental case. We have shown that the obtained similarity solutions, accounting also for the initial conditions in each case, generally agree well with the experimental results even in the near field. The results also show that the mean velocity of the transitional wake behind a tapered edge becomes self-similar almost immediately downstream of the edge.

1. Introduction

Although many aspects of sink flow have been studied in the literature (e.g. Pohlhausen 1921; Jones & Launder 1972; Sreenivasan 1982; Spalart 1986; Jones, Marusic & Perry 2001; Parsheh, Brown & Aidun 2005; Brown, Parsheh & Aidun 2006) evolution, influence of initial conditions on wake development and self-similarity of wakes in sink flow have not been thoroughly studied thus far. In addition to the fundamental importance of wakes in sink flow, they can also be found in a wide range of engineering applications, such as in the paper-manufacturing process. Can a flat-plate wake originating from a relaminarized boundary layer in sink flow become self-similar? What is the effect of the degree of boundary layer relaminarization on the wake evolution? Do such wakes become fully turbulent? The width of wakes in sink flow approaches zero at the sink; however, its evolution towards zero has not been determined thus far. What is the rate of decay of the velocity defect? This paper is devoted to investigating these issues.

† Email address for correspondence: ad@mech.kth.se

Substantial changes in the characteristics of wakes in straining flows have been reported in the literature (e.g. Elliott & Townsend 1981; Rogers 2002, 2005). In addition, aspects of wakes subjected to pressure gradients such as similarity state (Reynolds 1962; Keffer 1965; Narasimha & Prabhu 1972; Prabhu & Narasimha 1972; Ghosal & Rogers 1997; Moser, Rogers & Ewing 1998) and wake characteristics (Elsner & Wilczynski 1976) have been subjects of extensive investigations. Elsner & Wilczynski (1976) analytically and experimentally showed that a favourable pressure gradient accelerates the decay of the velocity defect, damps the turbulent fluctuations and makes the turbulence isotropic. As a result, the evolution of wake width is affected by the free-stream pressure gradients. It is well known that the width of wakes subjected to a favourable pressure gradient decreases downstream, whereas with an adverse pressure gradient it can exhibit a considerable growth rate (Gartshore 1967). A large adverse pressure gradient can cause local flow reversal or even wake burst (Hoffenberg, Sullivan & Schneider 1995). Hunt & Eames (2002) analytically studied evolution of wakes subjected to a constant mean rate of strain and found that the vorticity in the wake cannot interact with the external flow and, thus, diffuses inside the wake. Subsequently, the vorticity decays rapidly due to its opposite sign at different sides of the wake centreline.

Traditional self-similar theories for shear layers are derived such that the solutions, valid for the flow in the far field, are not explicitly functions of the initial conditions. Narasimha (1989) put forward as one of the five hypotheses for turbulent flows that such flows evolve asymptotically to a state independent of all details of their generation in spite of strong dependence in the near field. Narasimha (1989) further argues that these working rules are valid under certain conditions, and in some particular flows they can be violated. The concept of equilibrium similarity for a turbulent shear flow is defined by Narasimha & Prabhu (1972), following the ideas of Townsend (1956). A turbulent flow is considered to be in equilibrium if the mean velocity and turbulent stresses exhibit similarity with scales which develop downstream in essentially the same way. George (1995) generalized the concept of equilibrium similarity and argued that the velocity and turbulent-stress scales do not need to develop in the same way. Self-similarity may be sustained in the averaged momentum equation without this assumption. Equilibrium is then restricted to solutions for which the scaled similarity distributions for mean velocity and Reynolds stresses are independent of initial conditions, a necessary condition also in the original classical definition. However, the velocity and length scales may still be dependent on initial conditions. In fact, George (1989, 1995) suggests that a turbulent flow can asymptotically depend on the initial conditions even far downstream of its origination, and equilibrium similarity theory can account for this asymptotic flow behaviour – see, for example, Johansson, George & Gourlay (2003). George & Davidson (2004) have provided a thorough discussion regarding the role of the initial conditions in asymptotic turbulent-flow behaviour as well as in equilibrium solutions. In the present study, we basically follow the generalized definition of equilibrium similarity by George & Davidson (2004). However, our experiments in the transitional regime show that the sum of the scaled laminar- and turbulent-stress distributions become self-similar, rather than the turbulent-stress distribution alone. Therefore, the definition of equilibrium similarity is slightly expanded to include also flows with considerable laminar stress. In addition, our experiments show that the development of the velocity, length and stress scales of wakes originating from a

relaminarized boundary layer in sink flow are asymptomatically dependent on the initial conditions.

Details of the approach to the equilibrium condition for sink-flow flat-plate wakes is unknown, although that of many other types of wakes subjected to pressure gradients has been examined. For example, Prabhu & Narasimha (1972) showed that for a wake behind a cylinder subjected to continuous favourable pressure gradient, the approach to the classical Townsend (1956) equilibrium condition is quite slow, and the wake develops into temporary equilibrium conditions which change with time. In addition, Narasimha & Prabhu (1972) showed that a wake behind a tapered edge subjected to an impulsive favourable pressure gradient undergoes a slow relaxation process before reaching final equilibrium. However in the absence of pressure gradients, Narasimha & Prabhu (1972) showed that a wake behind a tapered trailing edge approaches equilibrium condition quite fast, whereas for a wake behind a cylinder it takes much longer time.

Narasimha & Prabhu (1972) derived a general self-similar solution for wakes subjected to arbitrary pressure gradients. Rogers (2002) conducted a comprehensive self-similarity analysis for wakes subjected to time-varying mean rates of strain with the mean external velocity changing as a power law and m as the scaling exponent. In this novel study, Rogers (2002) derived self-similar solutions for the functional forms of rates of strain for which self-similarity states exist. Based on this analysis, when $m = -1$ the resulting self-similar solution corresponds to the flow in the vicinity of the centreline of planar contractions.

In the present paper, we study the rapid approach of sink flow wakes towards the equilibrium conditions, in the sense of George & Davidson (2004). To do that, a more general equilibrium similarity solution is derived, as briefly discussed previously, in which we study the simultaneous presence of both laminar and turbulent stresses. This is of interest, since the boundary layer at the plate relaminarizes at sufficiently large acceleration numbers. Thus, the evolution of the wakes behind the tapered trailing edges are transitional. Only in one flow case, using a blunt trailing edge, the flow develops into a fully turbulent wake flow. We also display the dependence of the wake development on the initial conditions, as imposed by different flow cases. This is manifested primarily by an empirically determined turbulent diffusivity characterizing each flow case and also by the explicit application of initial conditions for quantities such as the momentum flux integral of the velocity defect and wake thickness. The derived equilibrium solutions are obtained in a cylindrical coordinate system such that the solution remains valid everywhere inside the planar contraction.

It is well known that relaminarized boundary layers are characterized by velocity fluctuations which do not affect the velocity profiles and even can be considered frozen (see e.g. Narasimha & Sreenivasan 1973, 1979; Talamelli *et al.* 2002). Subsanchandar & Prabhu (1998) showed that the near wakes of flat plates contain footprints of the upcoming boundary layer. Therefore, it is of particular interest to examine the effect of the fluctuations from the upcoming relaminarized boundary layers. In the experiments, a fully turbulent boundary layer along a flat plate in a contraction relaminarizes at the trailing edge. Possible footprints of the velocity fluctuations in the boundary layers of the plate are accounted for by using a more general assumption for the Reynolds-stress model in the wake than the standard one which considers a constant turbulent diffusivity. This increases the degree of freedom in the model for the shape of the velocity-defect profile.

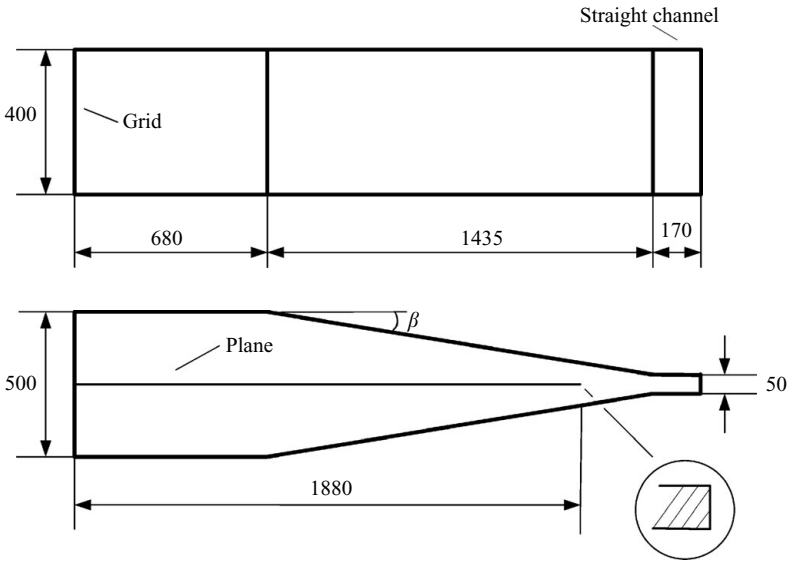

FIGURE 1. The schematic of the experimental set-up. The plate configuration corresponds to case I, and all dimensions are in mm.

2. The experiments

The experiments are carried out in a small wind tunnel in which the test section is replaced by a planar contraction with two constant cross-section channels attached to its inlet and outlet, shown in figure 1. Both the upper and lower walls of the test section are made of single pieces of 12 mm thick Plexiglas. The intersections of the contraction and the straight channels are formed by grooving each sheet to make 20 mm wide lines of thin material at two positions and bending the thinned sections into the specified angles. Therefore, flow separation at these intersections is prevented, which is verified by visualizing the flow using tufts. The measured velocity profiles across the channel cross-section at these regions showed that there were no sudden changes in the velocity field. Through a 20 mm wide streamwise slit at the upper wall, the measurement equipment enters the test section. The vertical traversing is performed using a micrometre with a resolution of 5 μm. The measurement equipment is traversed in the streamwise direction, using a linear traversing system. The contraction half-angle β is 8.9°, and the ratio of the outlet to inlet height is $C = 10$.

In order to generate a turbulent boundary layer at the contraction inlet, free-stream turbulence is produced by a grid (figure 1). The grid is of the form of biplane square-mesh arrays of square bars. The mesh size and bar diameter are 34 and 6 mm, respectively, resulting in a solidity of 0.32. To generate homogeneous, isotropic turbulence at the contraction inlet, the grid is placed 20 mesh size upstream of the inlet.

The velocity is measured using constant-temperature hot-wire anemometry (CTA). The diameter and length of the wires are 5 μm and 1.25 mm, respectively. The hot wires operate at 45 % overheat and are calibrated using a Pitot tube in the constant height channel. Wakes behind a blunt and a tapered edge are measured. For both edges, a 5.5 mm thick plate is placed at the contraction centreline. The tapered edge is provided by tapering the plate edge. The tapered half-angle and length are 4.1° and 35 mm, respectively. The effective thickness of the plate at the edge is 0.5 mm.

Case	r_1 (mm)	R_c	$\mathscr{I}_1$ (m^2 s^{-2})	b	m	$\sqrt{Re}\Phi_{w,1}$	Edge type
I	395	0.40	0.260	35	70	2.24	Blunt
II	395	0.40	0.132	0.20	28	1.24	Tapered
III	295	0.54	0.244	0.15	9.0	1.40	Tapered
IV	245	0.64	0.354	0.10	6.5	1.36	Tapered
V	205	0.76	0.524	0.06	4.5	1.44	Tapered

TABLE 1. Summary of the experimental cases: $R_c = r_c/r_1$ is the position of the contraction outlet, where r_1 and r_c denote the distances from the origin of the cylindrical coordinate system to the plate trailing edge and the contraction outlet, respectively; $\mathscr{I}_1$ and $\Phi_{w,1}$ denote estimated values at the edge, respectively; and b and m are the coefficient of the line fitted to $\tilde{\nu}_T(R)$ (see (4.1)); in all cases $Re = 160\times10^3$, and the Launder acceleration factor $K = 1/Re = 6.25\times10^{-6}$.

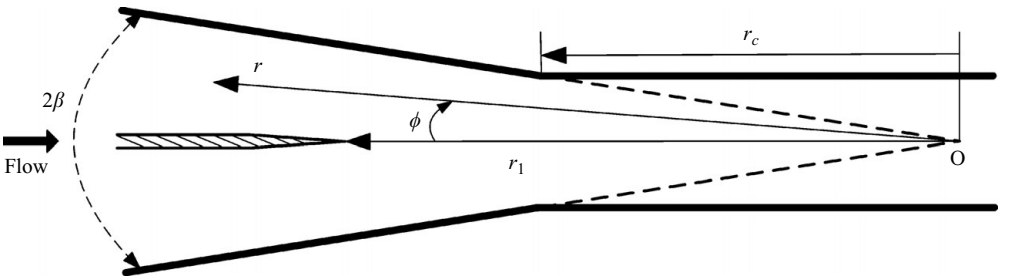

FIGURE 2. Scaled schematic of the experimental set-up and the coordinate system. Plate configuration corresponds to case IV.

In our analyses, we have used a cylindrical coordinate system (r, ϕ, z) located at the sink pointing against the flow direction as shown in figure 2. The corresponding velocity components are $(U_r + u_r, U_\phi + u_\phi, U_z + u_z)$, where the upper and lower cases denote the mean and fluctuating velocity components, respectively. In table 1, the experimental cases covered in this study are summarized.

3. Evolution of flat-plate wakes in sink flow

We are interested in deriving a general solution which is valid everywhere in a sink flow. Therefore, we have used a cylindrical coordinate system (r, ϕ, z) located at the sink to cover the flow in the entire contraction. The external undisturbed mean-velocity components outside the wake and the boundary layer of a thin flat plate become $\boldsymbol{U_E} = (U_r^e = -Q/2\beta r,\ U_\phi^e = 0,\ U_z^e = 0)$, where Q denotes the flow rate per unit width. The Reynolds number defined as $Re = -U_r^e r/\nu = Q/2\beta\nu$ is independent of r, where ν is the kinematic viscosity. For large Re, U_r^e is, to the lowest order, also the external-flow velocity component of thin wakes. Applying boundary-layer approximations, the momentum and continuity equations for the wake become

$$U_r\frac{\partial U_r}{\partial r} + \frac{U_\phi}{r}\frac{\partial U_r}{\partial \phi} - U_r^e\frac{\mathrm{d}U_r^e}{\mathrm{d}r} = \frac{1}{r}\frac{\partial}{\partial\phi}\left[\frac{\nu}{r}\frac{\partial U_r}{\partial\phi} - \overline{u_r u_\phi}\right], \tag{3.1}$$

$$\frac{1}{r}\frac{\partial}{\partial r}(rU_r) + \frac{1}{r}\frac{\partial U_\phi}{\partial\phi} = 0, \tag{3.2}$$

respectively, where $U_r = U_r^e + U_w$ is the wake velocity and U_w is the wake-velocity defect, and in shallow wakes $U_w \ll |U_r^e|$.

Let us consider a control volume which starts from the position r, extends upstream to infinity and lies between the two angles $\pm\Delta\phi$, where $\Delta\phi$ is large enough to enclose the wake. For small $\Delta\phi$, the momentum balance is given by

$$\int_0^{\Delta\phi} r\rho {U_r}^2 \mathrm{d}\phi - \int_r^{\infty} \rho U_r^e U_\phi \mathrm{d}r = -\frac{\mathscr{D}}{2} + \int_0^{\Delta\phi} r\rho U_r^{e2} \mathrm{d}\phi, \tag{3.3}$$

where $\mathscr{D}$ is the drag on the plate. Using (3.2), we can derive an expression for U_ϕ, which is used to derive the following relationship for the second term on the left-hand side of (3.3):

$$\int_r^{\infty} \rho U_r^e \frac{\mathrm{d}}{\mathrm{d}r}\left[r\int_0^{\Delta\phi}\left(U_r^e - U_r\right)\mathrm{d}\phi\right]\mathrm{d}r = r\rho U_r^e \int_0^{\Delta\phi}\left(U_r^e - U_r\right)\mathrm{d}\phi\Big]_r^{\infty} - \int_r^{\infty} \rho U_r^e \int_0^{\Delta\phi}\left(U_r^e - U_r\right)\mathrm{d}\phi\mathrm{d}r. \tag{3.4}$$

Considering the displacement and momentum loss angles, defined as

$$\Phi_d(r) = \int_0^{\infty}\left(1 - \frac{U_r}{U_r^e}\right)\mathrm{d}\phi; \qquad \Phi_m(r) = \int_0^{\infty}\frac{U_r}{U_r^e}\left(1 - \frac{U_r}{U_r^e}\right)\mathrm{d}\phi, \tag{3.5}$$

respectively, and defining $\mathscr{I} \equiv \Phi_d(r){U_r^e}^2$, (3.4) reduces to

$$\frac{\mathscr{D}}{2} = \rho r\mathscr{I}(r) - r\rho\int_0^{\infty} U_w^2 \mathrm{d}\phi + \rho\int_r^{\infty}\mathscr{I}\mathrm{d}r. \tag{3.6}$$

Differentiating (3.6) with respect to r and setting $\mathrm{d}\mathscr{D}/\mathrm{d}r = 0$ gives

$$\frac{\mathrm{d}}{\mathrm{d}r}\left[r\mathscr{I}(r)\right] - \frac{\mathrm{d}}{\mathrm{d}r}\left(r\int_0^{\infty} U_w^2 \mathrm{d}\phi\right) = \mathscr{I}(r). \tag{3.7}$$

For a shallow wake, the second term on the left-hand side of (3.7) is a factor of U_w/U_r^e smaller than the other two terms, and thus, $\mathrm{d}(r\mathscr{I})/\mathrm{d}r = \mathscr{I}$. This implies that $\mathscr{I}$ which can also be formulated as

$$\mathscr{I} \equiv -\int_0^{\infty} U_r^e U_w \mathrm{d}\phi = \mathscr{I}_0, \tag{3.8}$$

is constant to the lowest order in shallow wakes. Since $\mathscr{D}$ is independent of r, (3.6) can be evaluated at $r = 0$ to derive a relationship between $\mathscr{I}(r)$ and the drag.

Conducting a scale analysis, we determine the order of magnitude of the terms on the left-hand side of (3.1) in terms of r_1, β, U_w and U_r^e, where r_1 is the distance from the sink to the trailing edge, (see figure 2). Considering a shallow wake, after neglecting quadratic terms in U_w, (3.1) becomes

$$\frac{\partial}{\partial r}\left(U_r^e U_w\right) = \frac{1}{r}\frac{\partial}{\partial\phi}\left(\frac{\nu}{r}\frac{\partial U_w}{\partial\phi} - \overline{u_r u_\phi}\right). \tag{3.9}$$

We seek similarity solutions to (3.9) of the form

$$U_w = U_w^c f(\eta), \qquad \eta = \frac{\phi}{\zeta(r)}, \tag{3.10}$$

where $U_w^c(r)$ and $\zeta(r)$ are U_w at the centreline and the wake angular scale, respectively. We define the wake's integral angular scale as

$$\Phi_w(r) \equiv \frac{1}{U_w^c}\int_0^{\infty} U_w \mathrm{d}\phi = \zeta(r)\int_0^{\infty} f(\eta)\mathrm{d}\eta. \tag{3.11}$$

Without loss of generality we set $\int_0^\infty f(\eta)\mathrm{d}\eta = 1$ which leads to $\Phi_w(r) = \zeta(r)$ and $\eta(r,\phi) = \phi/\Phi_w(r)$. Applying (3.10) to (3.8) results in $U_w^c(r)\Phi_w(r) = 2\beta r\mathscr{I}_0/Q = -\mathscr{I}_0/U_r^e$.

In the following analysis, we consider that laminar and turbulent stresses are simultaneously present and $\overline{u_r u_\phi}$ consists of two parts given by

$$-\overline{u_r u_\phi} = \kappa_1(r) r\Phi_w U_w^c(r)\frac{1}{r}\frac{\partial U_w}{\partial\phi} + \kappa_2(r)\frac{(r\phi)^2}{r\Phi_w}U_w^c(r)\frac{1}{r}\frac{\partial U_w}{\partial\phi}, \tag{3.12}$$

where $\kappa_1(r)$ and $\kappa_2(r)$ are the scaling parameters for the terms corresponding to the mixing lengths typical for free shear layers and wall-bounded flows, respectively. This means that in addition to the turbulent fluctuations represented on average by the first term on the right-hand side of (3.12), we assume that other turbulent wake disturbances, for which $u_\phi = 0$ at $\phi = 0$, exist as well. The second term will add a degree of freedom to control the shape of the similarity profile. Unlike for fully turbulent wake flows in which the scaling parameter for mixing lengths is usually considered a constant, $\kappa_1(r)$ and $\kappa_2(r)$ are empirical functions of r. This means that the turbulence level can increase downstream. We note that the terms in (3.12) represent the simplest possible mixing-length models available. A more comprehensive model would take the eddy diffusivity proportional to the magnitude of local velocity gradient. Here, the velocity gradient is estimated by the ratio $U_w^c/(r\Phi_w)$. As a result, the effective eddy diffusivity of the second term will not be finite as ϕ increases. It is possible to implement the local magnitude of the velocity gradient in the eddy diffusivity, but it does not allow closed-form solutions, as the resulting equation is nonlinear. Therefore, we rather adhere to the simplicity of (3.12), keeping in mind the inaccuracy of the model for large values of ϕ. Considering (3.10) and η, we can rewrite (3.12) as

$$-\overline{u_r u_\phi} = U_w^{c\,2}(\kappa_1(r) + \kappa_2(r)\eta^2)\frac{\mathrm{d}f}{\mathrm{d}\eta}, \tag{3.13}$$

where f is the similarity function for transitional wakes that we seek to derive. Let us define non-dimensional laminar and turbulent stresses as

$$\tilde{\tau}_L = \frac{(\nu/r)(\partial U_w/\partial\phi)}{\nu U_w^c/r\Phi_w} = \frac{\mathrm{d}f}{\mathrm{d}\eta}, \qquad \tilde{\tau}_T = (\kappa_1 + \kappa_2\eta^2)\frac{Re\mathscr{I}_0}{U_r^{e2}}\frac{\mathrm{d}f}{\mathrm{d}\eta}, \tag{3.14}$$

respectively. We then introduce the non-dimensional turbulent-diffusivity coefficients $\tilde{\nu}_T$ and $\tilde{\xi}_T$ which are unknown functions of r, as $\tilde{\nu}_T(r) = Re\mathscr{I}_0\kappa_1(r)/U_r^{e2}$ and $\tilde{\xi}_T(r) = Re\mathscr{I}_0\kappa_2(r)/U_r^{e2}$, respectively, where both are $O(1)$ in transitional wakes.

We consider cases in which the initial turbulent and laminar stresses are of the same order of magnitude, and therefore, the non-dimensional total stress $\tilde{\tau}_s$ can be formulated as

$$\tilde{\tau}_s = \frac{(\nu/r)(\partial U_w/\partial\phi) - \overline{u_r u_\phi}}{\nu U_w^c/r\Phi_w} = (1 + \tilde{\nu}_T(r) + \tilde{\xi}_T(r)\eta^2)\frac{\mathrm{d}f}{\mathrm{d}\eta}. \tag{3.15}$$

Inserting (3.13) into (3.9) and using the definitions of $\tilde{\nu}_T(r)$ and $\tilde{\xi}_T(r)$ given above, we can show

$$R\Phi\Phi'\frac{\mathrm{d}(\eta f)}{\mathrm{d}\eta} = \frac{\mathrm{d}[(1 + \tilde{\nu}_T(R) + \tilde{\xi}_T(R)\eta^2)\mathrm{d}f/\mathrm{d}\eta]}{\mathrm{d}\eta}, \tag{3.16}$$

where $\Phi_w = \Phi/\sqrt{Re}$, $R \equiv r/r_1$, and the 'prime' denotes differentiation with respect to R. In order that similarity solutions exist, we require that the total stress has a self-similar shape. Thus, from (3.15), $\tilde{\xi}_T(R) = \gamma^2[1 + \tilde{\nu}_T(R)]$, where γ is an empirical

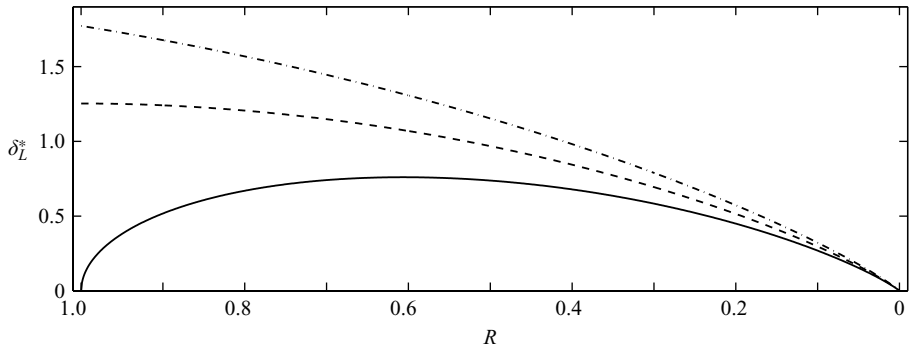

FIGURE 3. Dimensionless wake half-width δ_L^* when $\Phi_{L,1} = 0$: (—), $\Phi_{L,1} = \sqrt{\pi/2}$: (- - -) and $\Phi_{L,1} = \sqrt{\pi}$: (- · -).

constant dependent only on Re. Therefore, $\tilde{\nu}_T(R)$ and $\tilde{\xi}_T(R)$ are not independent functions if similarity prevails. As a result, the final condition for self-similarity reads

$$R\Phi\Phi' = -\alpha^2\left[1 + \tilde{\nu}_T(R)\right]. \tag{3.17}$$

The general solution for the wake angular scale becomes

$$\Phi(R) = \sqrt{(\Phi_1)^2 + 2\alpha^2\left[\ln\left(\frac{1}{R}\right) + \int_R^1 \frac{\tilde{\nu}_T(R)}{R}\mathrm{d}R\right]}, \tag{3.18}$$

where α^2 is determined based on the normalization condition and Φ_1 is the initial angular scale. The solution to (3.16) becomes

$$f = (1 + \gamma^2\eta^2)^{-\alpha^2/2\gamma^2}, \tag{3.19}$$

which represents a whole class of similarity solutions using different values of the free parameter γ. If γ is independent of initial conditions, f represents an equilibrium similarity solution in the generalized sense described previously. Whether γ is dependent on initial conditions or not, we cannot derive γ from the present analysis. Thus, it can only be determined from the experiments. In the limit when $\gamma \to 0$ (and using the normalization condition $\int_0^\infty f\mathrm{d}\eta = 1$) (3.19) reduces to the Gaussian $f_0 = \mathrm{e}^{-\pi\eta^2/4}$ with $\alpha^2 = \pi/2$. This limit covers also the laminar case for which $\gamma = 0$ and $\tilde{\nu}_T = 0$. Equation (3.16) then simplifies to $R\Phi_L\Phi_L' = -\alpha^2 = -\pi/2$, and thus, the wake angular scale becomes

$$\Phi_L = \sqrt{\Phi_{L,1}^2 + \pi\ln\left(\frac{1}{R}\right)}. \tag{3.20}$$

If the wake half-width is defined as $\delta = r\Phi_w$, the non-dimensional half-width can be presented as

$$\delta^* = \frac{\delta}{r_1 Re^{-1/2}} = R\sqrt{(\Phi_1)^2 + 2\alpha^2\left[\ln\left(\frac{1}{R}\right) + \int_R^1 \frac{\tilde{\nu}_T(R)}{R}\mathrm{d}R\right]}. \tag{3.21}$$

Equation (3.21) shows that the evolution of wake half-width is dependent on its initial value, $\Phi_1 = \delta_1/(r_1 Re^{-1/2})$. The relative importance of the initial value decreases slowly downstream as δ approaches zero. This is shown in figure 3 in which the non-dimensional wake half-width with different initial values is presented for the laminar

case. When $\Phi_{L,1} < \Phi_{L,c}(\equiv \sqrt{\pi/2})$ the wake half-width first increases to a peak and thereafter decreases towards zero at the sink, whereas if $\Phi_{L,1} > \Phi_{L,c}$, δ_L^* decreases monotonically downstream. Thus, the wake width increases if the wake angular scale is smaller than a threshold, whereas if the angular scale is sufficiently large it decreases. Since the wake angular scale increases monotonically downstream, initially thin wakes exhibit a peak in the wake width. Physically this can be described by the balance of the forces in the shallow wake, representing the small departure from the inviscid balance in the converging flow. When the wake angular scale is large, viscous and counterbalancing inertial forces are small, and accordingly the wake angle growth rate is weak. Therefore, the wake width follows qualitatively the inviscid streamlines of the converging flow. When the wake angular scale is small, viscous forces are much larger, thus requiring a significant wake-angle growth rate to maintain the balance with the inertial force. As a result, the wake width increases downstream. In a consistent manner, Prabhu, Narasimha & Sreenivasan (1974) observed that wakes subjected to a large favourable pressure gradient follow ideal-fluid solutions, and the wake width decreases downstream. The evolution of the wake half-width depicted in figure 3 and discussions presented above in principle also carry over to the turbulent case.

For our general case the scaled non-dimensional total stress is given by

$$\tau_s^* = \frac{\tilde{\tau}_s}{[1+\tilde{\nu}_T(R)]} = (1+\gamma^2\eta^2)\frac{\mathrm{d}f}{\mathrm{d}\eta}, \tag{3.22}$$

suggesting that τ_s^* has a universal shape, provided that γ is independent of initial conditions. Indeed, comparisons with our experiments, presented in § 4, show that γ can be considered constant, independent of the various initial conditions covered in this study. Thus, the shape of the self-similar profiles for the wake velocity and total stress are universally independent of the initial conditions, and only the magnitudes of the scaling parameters $U_w^c(R)$ and $\nu U_w^c(R)[1+\tilde{\nu}_T(R)]/r\Phi_w(R)$ depend on R. These functions of R are highly dependent on the initial conditions. This will be clarified below from the procedure for determining the scale factor $[1+\tilde{\nu}_T(R)] = 1 + Re\mathscr{I}_0\kappa_1(R)/U_r^{e2}$, which is basically based on finding the best agreement between (3.22) and the total-stress profiles of experiments with different initial conditions. Therefore, we may consider this similarity solution as an equilibrium solution in analogy with the generalized definition of equilibrium shear flows defined by George (1995). However, it should be noted that the derived equilibrium solution in this study is slightly different to the defined equilibrium solution by George (1995), as here the total stress profile, instead of the Reynolds shear stress, is self-similar.

Since $\tilde{\tau}_T = \tilde{\tau}_s - \mathrm{d}f/\mathrm{d}\eta$, we can show that the scaled Reynolds stress τ_T^* becomes

$$\tau_T^* = \frac{\tilde{\tau}_T}{[1+\tilde{\nu}_T(R)]} = \gamma^2\eta^2\frac{\mathrm{d}f}{\mathrm{d}\eta} + \frac{\tilde{\nu}_T(R)}{[1+\tilde{\nu}_T(R)]}\frac{\mathrm{d}f}{\mathrm{d}\eta}. \tag{3.23}$$

Therefore, there is no scaling factor that generally makes the shape of the Reynolds-stress profile independent of R. For tapered edges, we will have $\tilde{\nu}_T(R \approx 1) \ll 1$, which gives

$$\tau_T^* \approx \gamma^2\eta^2\frac{\mathrm{d}f}{\mathrm{d}\eta}, \tag{3.24}$$

and further downstream, i.e. $R \to 0$, we can assume that $\tilde{\nu}_T \gg 1$, which results in $\tau_T^* \approx \tau_s^*$, i.e. (3.22). Thus, the shape of the non-dimensional Reynolds-stress profile τ_T^* changes from the shape given by (3.24) to (3.22) when the flow develops downstream.

Using the shallow-wake approximations, the true initial conditions for both Φ_w and U_w^c cannot be fulfilled simultaneously, since the constant product $\mathscr{I}_0 = -U_r^e(R)U_w^c(R)\Phi_w(R)$ refers to a value downstream in the shallow wake that differs from $\mathscr{I}_1$ at $R = 1$. The relative sensitivity of Φ_w to its initial value decreases downstream, as is evident from (3.18). However, for a successful comparison of the analysis with the experiments, it is crucial to account for these initial values in the near field. Therefore, we present a procedure which is based on the similarity functions of shallow wakes in which the corrections to Φ_w and U_w^c, which satisfy the true initial conditions, are obtained by using the momentum integral analysis presented above. This involves also the determination of the function $\mathscr{I}(R)$, which is not assumed constant. The initial condition for the velocity defect is obviously $U_w^c(R = 1) = -U_{r,1}^e$. Observe that this does not imply that we can prescribe an initial condition for the detailed velocity profile. Let us define the wake initial width $\Phi^1(R = 1) = \Phi_w^1(R = 1)\sqrt{Re}$, where the superscript '1' denotes the distinction between the first-order solution $\Phi^1(R)$ and the zeroth-order solution $\Phi(R)$ as already given by (3.18). With these initial conditions, we also have $\mathscr{I}(R = 1) = \mathscr{I}_1 = (U_{r,1}^e)^2\Phi_w^1(R = 1)$ which concludes the set of required initial conditions.

The zeroth-order solution is obtained from the assumption that $\mathscr{I} = \mathscr{I}_0$, where $\mathscr{I}_0 = -U_r^e U_w^c \Phi/\sqrt{Re}$. Thus

$$\frac{U_w^c(R)}{U_w^c(R = 1)} = \frac{\mathscr{I}_0}{\mathscr{I}_1}\frac{\Phi^1(R = 1)}{\Phi(R)}R, \tag{3.25}$$

which provides the solution to the velocity defect, where $U_{r,1}^e/U_r^e = R$. We still have the freedom to specify the fictive initial condition for the zeroth-order solution, Φ_1. This value is chosen such that the initial condition for U_w^c is fulfilled. Then, since at $R = 1$ the left-hand side of (3.25) is equal to unity, we find $\Phi_1 = \mathscr{I}_0\Phi^1(R = 1)/\mathscr{I}_1$. The value of $\mathscr{I}_0$ is unknown *a priori* but will be determined as part of the solution for $\mathscr{I}(R)$ later. The first-order solution, $\Phi^1(R)$, is obtained from the definition of $\mathscr{I}(R) = -U_r^e U_w^c \Phi^1(R)/\sqrt{Re}$. Therefore, we can show

$$\frac{\mathscr{I}(R)}{\mathscr{I}_1} = \frac{U_w^c(R)\Phi^1(R)}{RU_{w,1}^c\Phi^1(R = 1)}, \tag{3.26}$$

which with (3.25) yields

$$\Phi^1(R) = \frac{\Phi(R)\mathscr{I}(R)}{\mathscr{I}_0}. \tag{3.27}$$

Thus, since $\mathscr{I}(R)$ asymptotically approaches $\mathscr{I}_0$ downstream, the first-order solution coincides with the zeroth-order solution there. Also, considering the first-order solution for $\Phi^1(R)$ together with the boundary condition for the zeroth-order solution for Φ_1, if $\mathscr{I}(R)$ satisfies its initial condition $\mathscr{I}(R = 1) = \mathscr{I}_1$, so will Φ^1 at $R = 1$. It remains to obtain the function $\mathscr{I}(R)$. By substituting the similarity assumptions, (3.10), into (3.7) and dividing by $\mathscr{I}_1$, we obtain

$$\frac{\mathrm{d}[\tilde{\mathscr{I}}(1 - R\tilde{U}_w F^2)]}{\mathrm{d}R} = \tilde{\mathscr{I}}\tilde{U}_w F^2, \tag{3.28}$$

where $\tilde{\mathscr{I}} = \mathscr{I}/\mathscr{I}_1$, $\tilde{U}_w = -U_w^c/U_{r,1}^e$ and $F^2 \equiv \int_0^\infty f^2 \mathrm{d}\eta$. The implicit solution to this equation which satisfies the initial condition $\tilde{\mathscr{I}}(R = 1) = 1$ is given by

$$\tilde{\mathscr{I}}(R) = \frac{1 - \tilde{U}_{w,1}F^2 - \int_R^1 \tilde{\mathscr{I}}\tilde{U}_w F^2 \mathrm{d}R}{1 - R\tilde{U}_w F^2}, \tag{3.29}$$

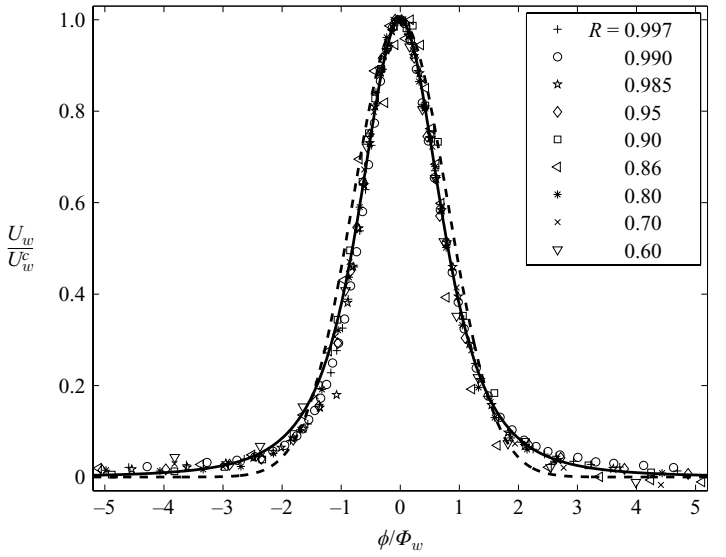

FIGURE 4. The mean-velocity profiles of case III in self-similar coordinates compared to the self-similar functions $f_0(\eta)$ (- - -) and $f(\eta)$ (–).

where $\tilde{U}_{w,1} = -U_w^c(R=1)/U_{r,1}^e = 1$ denotes normalized velocity defect at the edge. Considering (3.25), $\tilde{U}_w(R)$ is a known function, except for the ratio $\tilde{\mathscr{I}}_0 = \mathscr{I}_0/\mathscr{I}_1$ which comes out as a part of the solution. An explicit solution to (3.29) can be obtained iteratively.

4. Results and discussion

We have summarized the experimental cases in table 1. In all cases $Re = 160 \times 10^3$ which results in an acceleration factor $K = 1/Re = 6.25 \times 10^{-6}$. Figure 4 shows the self-similar model functions $f_0 = \mathrm{e}^{-\pi\eta^2/4}$ and f, compared to the mean-velocity-defect profiles of case III in the similarity coordinates. The free parameter, γ, of the second model function, f, represents the magnitude of the primary turbulent-diffusivity coefficient $\tilde{\xi}_T$. The best fit to the experimental data was obtained when $\gamma = \pi/3.8$ and $\alpha = 1.6$, where the latter was determined by the normalization condition for f. With these values of the parameters, f is narrower in the peak and wider at the tails than f_0 and, thereby, agrees better with the experiments. Comparing f_0 and f for other cases, we found that f, with the same values of $\gamma = \pi/3.8$ and $\alpha = 1.6$, agrees better with the mean-velocity-defect profiles in all of them. This particular velocity profile appears to be a universal model function for the diverse range of initial conditions considered at this Re. The good agreement between f and the experiments is due to the additional Reynolds-stress term, accounting for the fluctuations similar to those in wall-bounded flows, which influences the mean-velocity profile significantly.

The turbulent-diffusivity coefficient $\tilde{\nu}_T$ is determined by fitting (3.22) to the total-stress profiles at each measurement position. This is done such that the peak of the total-stress profile, τ_s^*, agrees with the peak of (3.22). The results are presented in figure 5. The shortest plate, used with both blunt and tapered edges, generates the largest overall level of $\tilde{\nu}_T$. This was expected, since the boundary layer at the edge of the shortest plate is characterized by the lowest degree of relaminarization. For this plate, $\tilde{\nu}_T$ increases at a much larger rate with the downstream distance from the

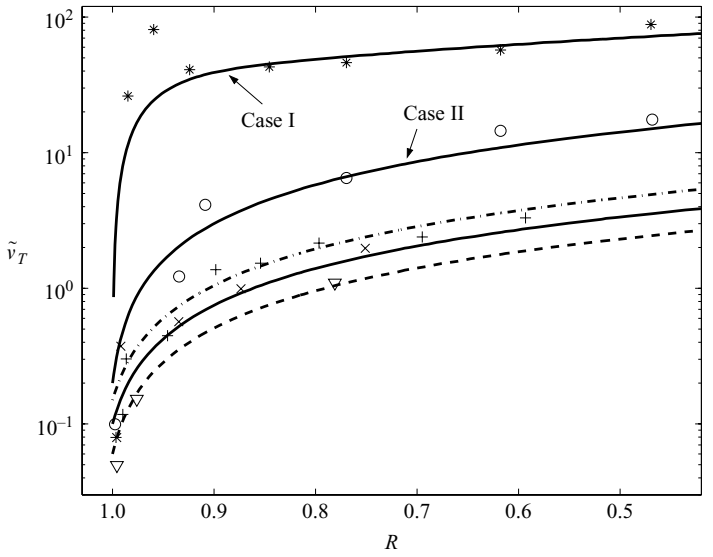

FIGURE 5. Downstream change of $\tilde{\nu}_T(R)$. Fitted curves: arrows show cases I and II; case III (- · -), IV (—) and V (- - -). Experiments: case I (∗), II (○), III (+), IV (×) and V (▽).

trailing edge. In particular, this is more profound for the blunt edge, case I, which rapidly reaches a state that can be classified as a fully developed turbulent case. For tapered cases, the overall level of $\tilde{\nu}_T$ gradually decreases with increasing plate length, as a response to the increase in the degree of relaminarization of the boundary layer. Apparently, the degree of relaminarization of the boundary layer at the edge can influence the characteristics of the whole wake, since the overall growth rate of $\tilde{\nu}_T$ versus $(1 - R)$ also decreases with increasing plate length. We have fitted curves to $\tilde{\nu}_T(R)$ to provide a rough analytical description of $\tilde{\nu}_T$ in each case, using

$$\tilde{\nu}_T(R) = b + m(1 - R) + [A + B(1 - R)]R^{20}. \tag{4.1}$$

The last term on the right-hand side of (4.1) is non-zero only in case I, which accounts for the rapid growth of $\tilde{\nu}_T$ close to the edge. In case I, $A = -35$ and $B = 100$, and in the other cases $A = B = 0$ which means that fitted $\tilde{\nu}_T$ reduces to a line. The values of b and m for all cases are presented in table 1.

Figure 6(a) shows profiles of U_w in case I compared with the model function f in the similarity coordinates. The first measured profile downstream of the edge shows traces of the two separated boundary layers at the blunt edge. The third measured profile at $R = 0.92$ and the profiles downstream of this position agree fairly well with f. Note that the effect of the edge shape is still present in the similarity-scaling parameters. Scaled total-stress profiles, τ_s^*, measured close to the edge also show traces of the separated boundary layers, as shown in figure 6(b). Although the scatter is larger here, a state fairly close to self-similar, τ_s^* seems to appear at $R \leqslant 0.85$, which can be compared to $R \leqslant 0.92$ for U_w. At $|\eta| > 0.6$ the agreement of τ_s^* with (3.22) is only qualitative. Scaled profiles of τ_T^* are shown in figure 6(c). As it is clear from figure 5, the increase of $\tilde{\nu}_T(R)$ behind the blunt edge is quite rapid, which means that the profiles of τ_s^* and τ_T^* are almost identical in this case, except in the first measurement position downstream of the edge.

Scaled profiles of U_w in the tapered cases are shown in figure 7 in which for all plate lengths, the profiles collapse into a single curve. To the accuracy that one can

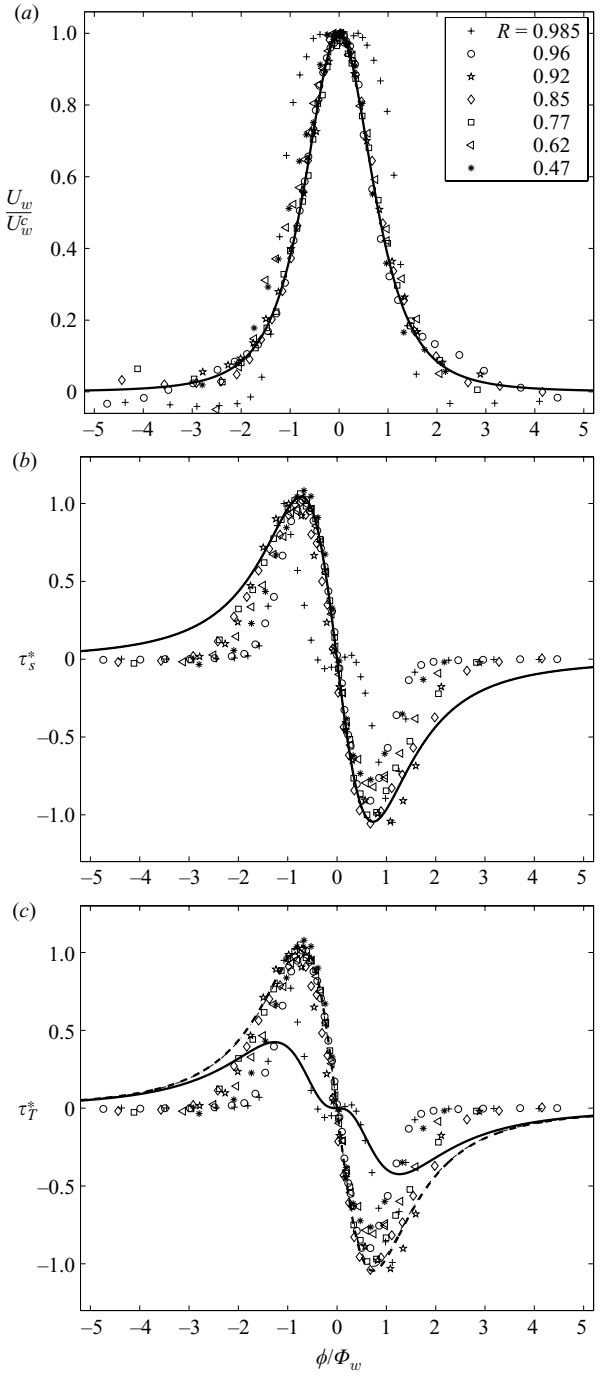

FIGURE 6. (*a*) Velocity profiles in similarity coordinates for case I and f (—). (*b*) Normalized total shear stress in similarity coordinates and $(1+\gamma^2\eta^2)\mathrm{d}f/\mathrm{d}\eta$ (—). (*c*) Non-dimensional Reynolds stress: (3.24) (—) and (3.22) (– – –).

infer from these profiles, this also includes the profiles immediately downstream of the edge. The merging boundary layers at the edge of the tapered cases correspond to a velocity defect which is qualitatively similar to f and differs from the velocity-defect

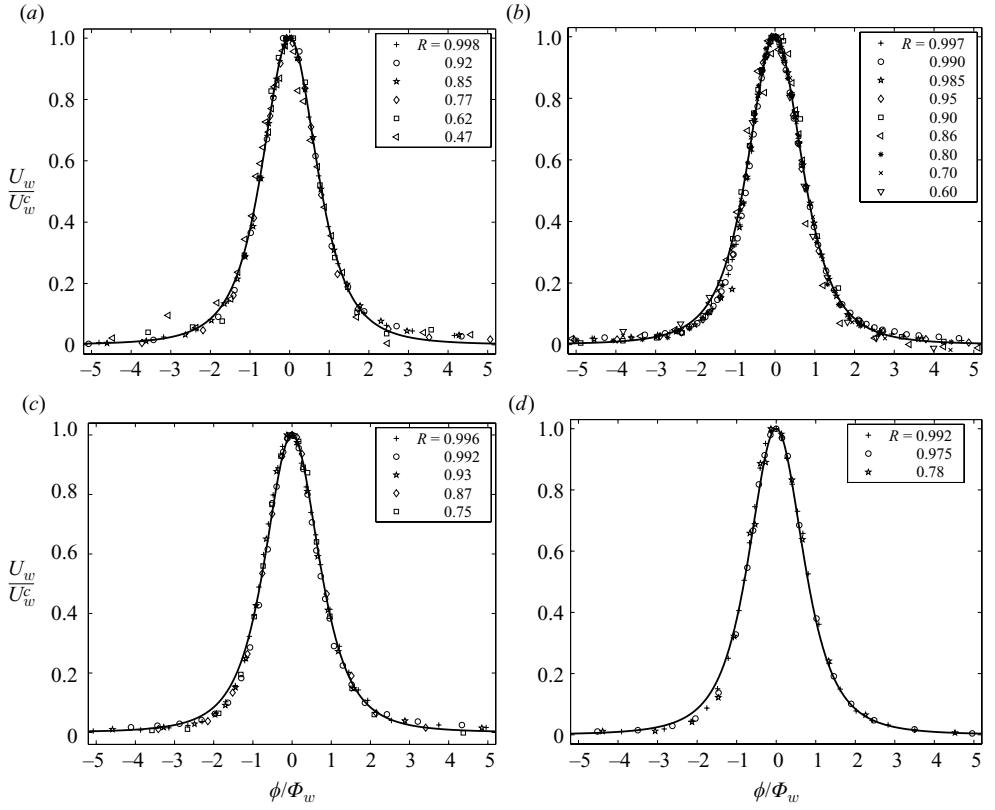

FIGURE 7. Mean-velocity profiles in similarity coordinates for (*a*) case II, (*b*) III, (*c*) IV and (*d*) case V.

profile corresponding to the case of separating boundary layers at a blunt edge. In both figure 6 (blunt case) and figure 7 (tapered cases) $\gamma = \pi/3.8$ and $\alpha = 1.6$, which means that these parameters are universal for all cases at this Re. Since the agreement of the wake-velocity defect with f is independent of upstream conditions, such as the state of the relaminarization of the boundary layer at the edge and even the initial wake velocity profile, f represents an equilibrium solution. In other words, the effect of the initial conditions is only included in the scaling parameters (George & Davidson 2004).

Figure 8 shows that the profiles of τ_s^* in tapered cases nearly collapse into a single curve, although it is far from conclusive for the velocity profiles. (The scatter in figure 8*b* represented by a few profiles will be discussed below.) The agreement with the self-similar solution, $[1+(\gamma\eta)^2]\mathrm{d}f/\mathrm{d}\eta$, is good only in the interval between the peaks. However, a qualitative agreement holds for the entire range of η. Note that the scaling procedure, which is based on fitting the peaks of the measured profiles to that of the self-similar profile, also contributes to the good agreement for small $|\eta|$. Comparing the results in figure 8 we find that the collapsing curves are not exactly the same in all cases. In case II, figure 8(*a*), the peaks of the measured profiles generally appear a little wider and closer to the analytical curve than the other cases. The differences are small, however, and the collapsing curves of figure 8(*b–d*) seem to represent more or less the same curve as shown in figure 9. Thus, we can conclude that for tapered cases the total stress profiles represent, at least approximately, one single curve.

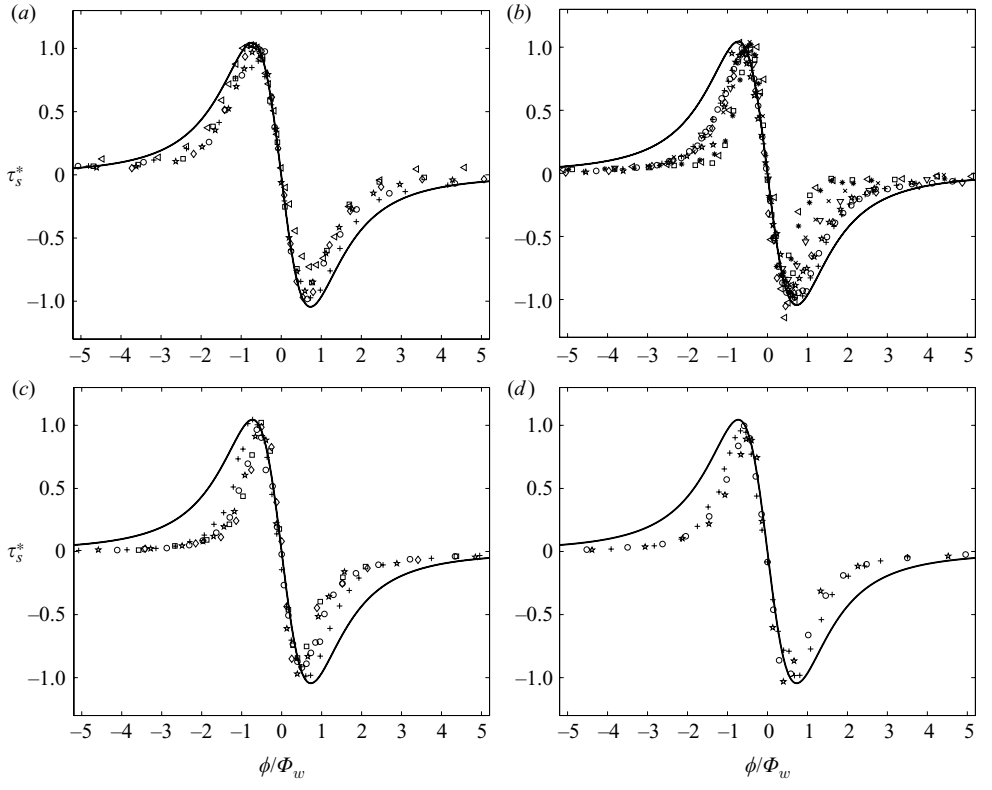

FIGURE 8. Normalized total-stress profiles in similarity coordinates and $(1+\gamma^2\eta^2)\mathrm{d}f/\mathrm{d}\eta$ (—) for (*a*) case II, (*b*) case III, (*c*) case IV and (*d*) case V; for symbols see figure 7.

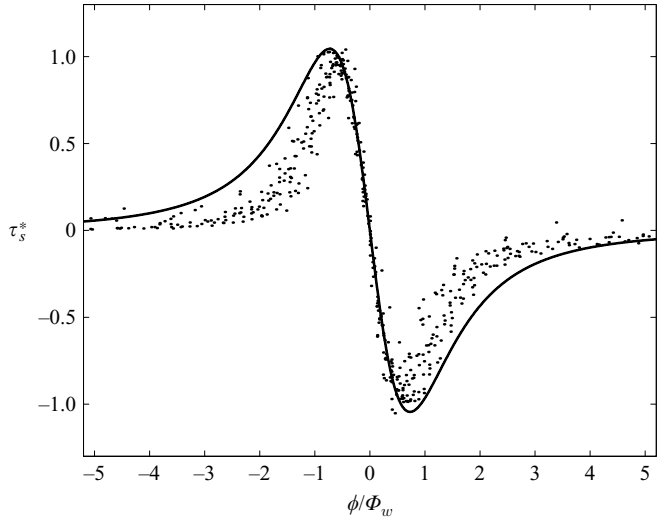

FIGURE 9. Total-stress profiles measured in cases II, III, IV and V except profiles at $0.8 \leqslant R \leqslant 0.9$ in case III (·) and (3.22) (–).

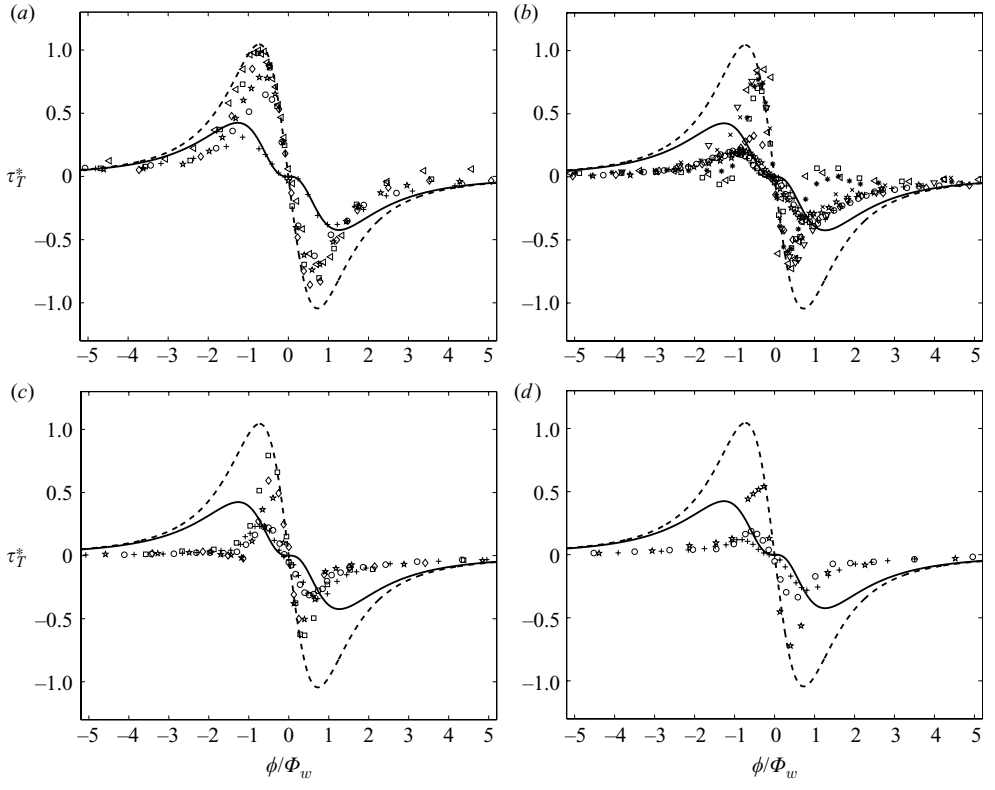

FIGURE 10. Non-dimensional Reynolds-stress profiles and the estimations based on (3.24) (—) and (3.22) (- - -) for (*a*) case II, (*b*) case III, (*c*) case IV and (*d*) case V; for symbols see figure 7.

Turning the attention to τ_T^*, shown in figure 10, we find that these profiles do not collapse into a single curve. Unlike the blunt case, in the tapered cases the increase of the turbulence level towards a fully developed state is fairly slow. As shown in figure 5, $\tilde{\nu}_T$ in these cases is of the order of unity or less in a wide range of R. Thus, when the laminar and turbulent stresses are of the same order of magnitude, the self-similarity state is available for the total stress rather than for τ_T^*. The changes of the shape of measured τ_T^* profiles appear to be consistent with the results of the self-similarity analysis. As figure 10 shows the τ_T^* profile changes from (3.24), valid at small $\tilde{\nu}_T$ and $\tilde{\xi}_T = \gamma^2$, to (3.22), valid for large $\tilde{\nu}_T$ and $\tilde{\xi}_T = \gamma^2\tilde{\nu}_T$. For the shortest plate, the degree of the relaminarization of the merging boundary layers at the edge is lower than the other cases. This can be the reason behind the approach of τ_T^* to a nearly developed turbulent state far downstream. In this region, the measured profiles almost collapse into a single curve. As shown by Narasimha & Sreenivasan (1973) the relaminarization process is asymptotic, and thus the degree of relaminarization at the trailing edge increases with plate length. Therefore, τ_T^* in longer cases, figure 10(*b–d*), never reaches fully turbulent state, and profiles of τ_T^* do not collapse into a single curve. However, we do not exclude the possibility that they might collapse into a single curve at positions farther downstream, which our existing experimental set-up does not cover. Immediately downstream of the edge where $\tilde{\nu}_T < 1$, the qualitative similarity of the measured profiles with (3.22) is clear, in particular, for small $|\eta|$.

This seems to hold for the first profiles measured behind the edge for all plate lengths.

A set of τ_s^* profiles in figure 8(b), at $R = 0.8$, 0.86 and 0.9 of case III, do not collapse into a single curve as the other profiles do. We conjecture that this is due to a local, weak departure from equilibrium because of some fundamental instability mechanisms in the wake, as e.g. inflectional instability of the velocity profile, or the appearance of some coherent structures emanating from vortex-shedding mechanisms at the edge. Further growth of the phenomenon appears to be bypassed by the rapid recovery of the wake in sink flow, since there is a return to self-similarity downstream. This appears to be nearly as fast as the approach to the self-similarity state behind the blunt edge. Alternatively, the instability/vortex structure breaks down to become just part of the overall-growing turbulence. Since the departure from the self-similarity of the total stress is fairly weak, it appears that this phenomenon does not have a considerable influence on the U_w profile shown in figure 7(b). Nevertheless, a magnification of the scales in figure 7(b) displays small deviations from the other profiles. Why does this departure from the self-similarity not appear in the other cases? We believe that this phenomenon might also be present in cases IV and V, although the effect is much weaker. Considering τ_T^* profiles of case IV in figure 10(c), at $R = 0.92$ and $R = 0.87$, a similar behaviour can be observed. The non-similar profiles in case III are characterized by a negative peak in τ_T^* at $\eta < 0$ and positive peak at $\eta > 0$. This peak is present also in figure 10(c), at least at $\eta < 0$, but is not as distinct as in figure 10(b). In case V the effect is presumably even weaker, although the available measurement stations might not cover the region in which this effect can be found. Neither are there any signs of such behaviour in the total-stress profiles of case II. In this case, it is likely that the instability is bypassed by the overall higher growth rate of the turbulence. Parsheh (2001) found that energy spectra of the vertical velocity fluctuations in the tapered cases show the presence of regular fluctuations with constant frequency throughout the wake. The relative magnitude of this fluctuation energy, as compared to the entire energy of fluctuations, initially increases but decreases further downstream. The blunt case shows a similar behaviour close to the edge but at a much larger magnitude.

Figure 11(a,b) shows the evolution of measured $\mathscr{I}(R)$ and $U_w^c(R)$, respectively. Also, the evolution of $\delta^*(R)$ for cases I and II and for cases III–V are shown in figures 11(c) and 11(d), respectively. These quantities are compared to their corresponding analytical results, calculated based on the extended analysis using the momentum integral analysis. The fitted curves to $\tilde{v}_T$, shown in figure 5, are used as approximate analytical expressions in these analyses. Figure 11(a) shows that $\mathscr{I}(R)$ decreases sharply near the plate edge and then becomes flat downstream. The length scale of the region of rapid decay is caught fairly well by the analysis. In addition, the flat region is predicted quite well. Figure 11(b) clearly shows a rapid recovery of the wake velocity inside the contraction, where the fastest recovery occurs in the fully turbulent case of a blunt edge. For the tapered edges and longer plates, the recovery is slower. The analysis seems to catch the relative rates of recovery of different cases fairly well. From figures 11(c)–(d) it is clear that the initial width of the wake in case I, blunt edge, is much larger than in the other cases. This was expected, since the wake width immediately downstream of the edge is the sum of the separating boundary layers and the plate thickness. Since the development of $\tilde{v}_T(R)$ in (3.18) is dependent on the initial conditions, although here implemented empirically in (4.1), the overall effect of changing the initial wake width remains even far downstream.

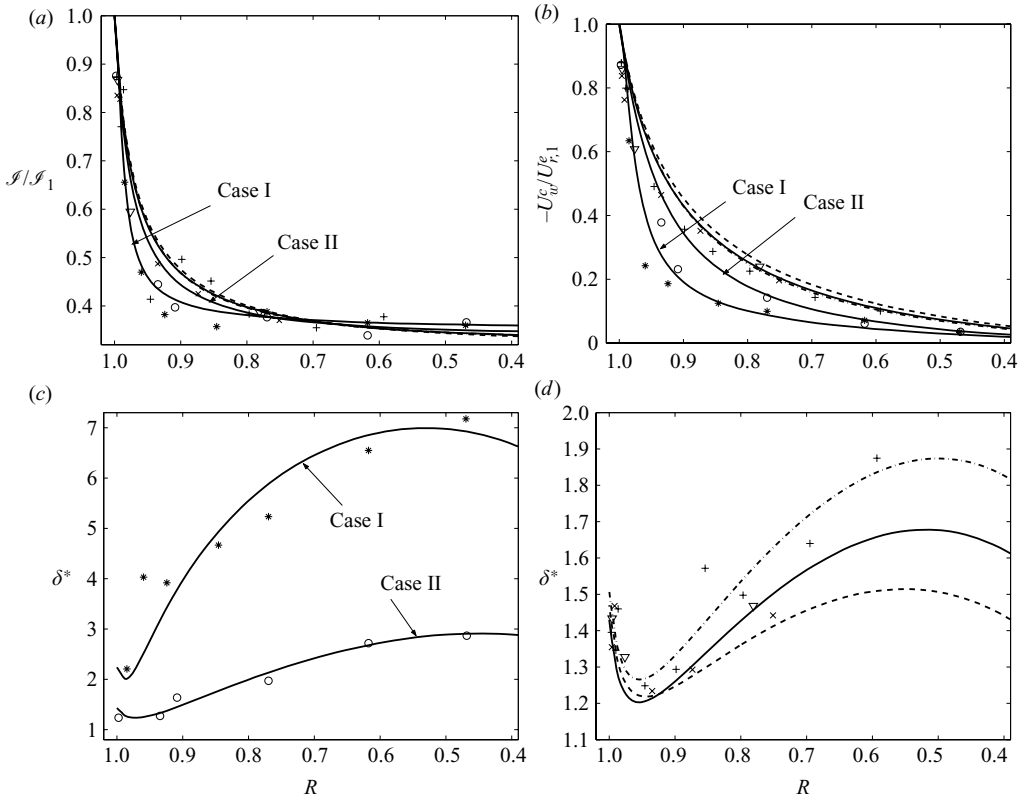

FIGURE 11. Downstream change of (*a*) $\mathscr{I}/\mathscr{I}_1$, (*b*) $-U_w^c/U_{r,1}^e$ and (*c*) δ^* in cases I and II and (*d*) δ^* in cases III, IV and V; symbols are the same as in figure 5.

We have also used the extended analysis to illustrate the separate sensitivity of the evolution of wake half-width to the changes to its initial value, artificially keeping $\tilde{\nu}_T(R)$ the same, independent of the initial conditions. In figure 12, δ_b^*/δ_a^* for cases I and III are presented, where δ_a^* and δ_b^* are calculated using δ_1^* and $1.5\delta_1^*$ as initial values, respectively, and δ_1^* is based on the experimental cases given in table 1. For the blunt case, δ_b^*/δ_a^* decreases sharply a short distance downstream of the edge and asymptotically approaches unity. For the tapered case III, the evolution of δ_b^*/δ_a^* is relatively more sensitive to the magnitude of the initial value. It is also clear from (3.18) that in the tapered cases the growth of Φ is slower, as the turbulent diffusivity in such cases is much smaller than in the blunt case. The relative importance of the initial value, Φ_1, is sustained for larger distances downstream in the tapered cases. It should be noted that any true physical change of the initial condition of the wake width also changes the development of $\tilde{\nu}_T(R)$, giving a different behaviour also far downstream. This is quite clear when comparing cases I and II in which the corresponding ratio of δ^* certainly does not asymptotically approach unity using the present empirical models of $\tilde{\nu}_T$. A complete asymptotic independence on the initial condition would require that $\tilde{\nu}_T(R)$ also approaches a universal behaviour far downstream. Considering the trend of the experimental data in figure 5 it does not seem very likely that it happens. However, we cannot completely exclude such scenario, since, indeed, there is a lack of data in the region $R < 0.5$. Note also that the general rule of asymptotic independence of initial conditions, suggested by Narasimha

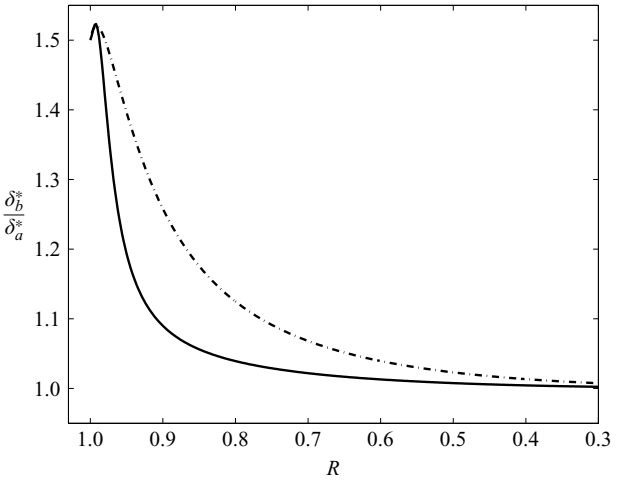

FIGURE 12. Evolution of the computed non-dimensional wake width, using different initial conditions; δ_b^* and δ_a^* are computed using $1.5\delta_1^*$ and δ_1^* as initial widths, respectively; case I (—) and case III (— · —).

(1989), relates to turbulent flows. However, in our experiments only case I with a blunt edge turned out to represent a fully turbulent flow. Therefore, our results do not really contradict with this working rule in a strict sense. The working rule would require $\tilde{\nu}_T$ to be asymptotically independent of the initial conditions in different fully developed flows, which is not considered here.

5. Conclusions

We studied the evolution of flat-plate wakes in sink flow both experimentally and theoretically. The experiments were performed at $Re = Q/2\beta\nu = 160 \times 10^3$, corresponding to a Launder acceleration parameter $K = 1/Re = 6.25 \times 10^{-6}$, which was much larger than the critical value required for the relaminarization of boundary layers in favourable pressure gradients. In the theoretical analysis, we derived equilibrium solutions for shallow wakes. It was found that the shape of the measured velocity-defect profile in the shallow region is universal in all experiments covered in this study and agrees well with the derived self-similar solution. This means that the shape of the shallow-wake velocity-defect profile is independent of the imposed initial conditions, such as the plate length and the type of the edge. A particular feature of wakes in sink flow is the quite rapid development towards the shallow-wake state. For tapered cases, it appeared that the shape of the scaled velocity-defect profiles collapsed well into a single curve even at $R = 0.99$. Partly, this might be an effect of the strong pressure gradient. In addition, the shape of the merging boundary layers on opposite sides of the plate represents a velocity defect at the edge which is not far from the wake itself. Nevertheless, the details of the U_w-profile at the edge do not seem to directly influence the similarity solution downstream, since the same shape appears in the blunt case, albeit at a relative position farther downstream.

In case I, a blunt edge, a short distance downstream of the edge, the Reynolds-stress profiles developed into a state that can be considered a fully developed turbulent wake. In addition, the corresponding turbulent-diffusivity coefficient, on a logarithmic

scale, appeared roughly independent of the downstream position. In the tapered cases, the magnitude of the turbulent stress was much smaller than the blunt case, but the relative growth rate was larger. In fact, in these cases the laminar and turbulent stresses were of the same order of magnitude in the near-wake region. However, the downstream growth rate of the turbulent-diffusivity coefficient decreased as the plate length was increased. This could be attributed to the initial condition of the wake, as influenced by the different degrees of relaminarization in the boundary layers at the edge of different plate lengths. We also found that in the cases in which the magnitude of the laminar and turbulent stresses are comparable, the existence of self-similar solutions naturally requires that the total-stress profile becomes self-similar. This means that the Reynolds-stress profile does not necessarily have a universal shape which is also confirmed by the experiments. To reproduce this behaviour in the theoretical model, the Reynolds-stress mixing-length model was required to involve an additional term as compared to the standard procedure in wake flows. This additional term uses a mixing length which is proportional to the distance from the wake centreline rather than a mixing length just related to the wake width. This approach not only enables us to demonstrate a non-universal shape of the Reynolds-stress profile in the similarity solution but also provides a better agreement with the measured velocity-defect profiles.

The additional contributing term to the Reynolds stress is typical for mixing-length models in wall-bounded flows. When the plate is long, in the near-wake region of the tapered edge, this term is the dominant contributor to the Reynolds shear stress and is of the order of magnitude of the laminar stress. Thus, turbulent stresses are present even in the very near-wake region which seems to be originating from the relaminarized boundary layer as shown by Narasimha & Sreevivasan (1973, 1979) and Talamelli *et al.* (2002). It is well known that this kind of low-level turbulent stresses are too weak to influence the velocity profile of the boundary layer. However, the wake, which has a different type of force balance at the centreline, is more susceptible to such stresses. In fact, if this additional stress term is cancelled in the Reynolds-stress model, the similarity profile of the velocity defect reduces to the traditional Gaussian profile, which does not agree well with the experiments. As an alternative to this hypothesis, we conjecture that there might be a local turbulent phenomenon around the edge which generates this stress, such as pairwise, simultaneous vortex shedding from the edge. Such a phenomenon would, however, be critically dependent on the edge shape.

Unlike the self-similar functions obtained for the velocity-defect and total-stress profiles which are universal, the magnitude of the velocity defect at the wake centreline, U_w^c, the stress scale, $\nu U_w^c[1 + \tilde{\nu}_T(R)]/r\Phi_w$, and the wake angle, Φ_w, are critically dependent on the initial conditions of the wake. In the model, the main reason for this dependency is the empirically determined turbulent diffusivity which develops differently for each flow case. Our primary analysis is based on the shallow-wake property that $\mathscr{I}$ is a constant. However, since this constant, $\mathscr{I}_0$, differs from the value of $\mathscr{I}$ at the trailing edge, it is not possible to relate the shallow-wake solution of the integral properties to the actual initial conditions of the wake. This is a considerable setback, since one cannot expect good agreement with the experiments in the near-wake region. Instead, a good agreement could only be obtained farther downstream. To overcome this problem we have developed an approximate solution method, based on the momentum integral equation, which allows us to use the true initial conditions of the integral properties of the wake. The only required inputs for this model are then the initial conditions of the integral properties and the empirically

determined scaling factor of the Reynolds stress, $\tilde{v}_T$, as a function of downstream distance. We then found reasonable agreement with the experiments in the near-wake region as well. The dependence on initial conditions of the measured wake angle and the magnitudes of the corresponding turbulent-diffusivity coefficient and stress seems to persist also far downstream of the edge, according to extrapolated trends of our results towards $R = 0$. Thus, we do not observe any asymptotic independence of initial conditions. However, we believe that such independence might appear only for fully turbulent wakes. In our measurements only one set of the initial conditions, case I, represents a fully turbulent case.

The experiments in this paper were sponsored by the PhD programme of FaxénLaboratoriet and is part of the doctoral thesis of the first author. The authors also wish to acknowledge the help of Dr Johan Westin, Mr Ulf Landén and Mr Marcus Gällstedt.

REFERENCES

Brown, M. L., Parsheh, M. & Aidun, C. K. 2006 Turbulent flow in a converging channel: effect of contraction and return to isotropy. *J. Fluid Mech.* **560**, 437.

Elliott, C. J. & Townsend, A. A. 1981 The development of a turbulent wake in a distorting duct. *J. Fluid Mech.* **113**, 433.

Elsner, J. W. & Wilczynski, J. 1976 Evolution of Reynolds stresses in turbulent wake-flows with longitudinal pressure gradient. *Rozpr. Inz.* **24** (4), 699.

Gartshore, I. S. 1967 Two-dimensional turbulent wakes. *J. Fluid Mech.* **30**, 547.

George, W. K. 1989 The self-preservation of turbulent flows and its relation to initial conditions and coherent structures. In recent *Advances in Turbulence* (ed. W. George & R. Arndt Hemisphere New York), p. 39.

George, W. K. 1995 Some new ideas for similarity of turbulent shear flows, In *ICHMT Symp. on Turbulence, Heat and Mass Transfer*, Lisbon, Portugal.

George, W. K. & Davidson, L. 2004 Role of initial conditions in establishing asymptotic flow behavior. *AIAA J.* **42** (3), 438.

Ghosal, S. & Rogers, M. M. 1997 A numerical study of self-similarity in a turbulent plane wake using large-eddy simulation. *Phys. Fluids* **9**, 1729.

Hoffenberg, R., Sullivan, J. P. & Schneider, S. P. 1995 Wake measurements in a strong adverse pressure gradient. *AIAA J.* **95**, 912.

Hunt, J. C. R. & Eames, I. 2002 The disappearance of laminar and turbulent wakes in complex flows. *J. Fluid Mech.* **457**, 111.

Johansson, P. V., George, W. K. & Gourlay, M. G. 2003 Equilibrium similarity, effect of initial conditions and local Reynolds number on the axisymmetric wake. *Phys. Fluids* **15** (3), 603.

Jones, W. P. & Launder, B. E. 1972 Some properties of sink-flow turbulent boundary layers. *J. Fluid Mech.* **56**, 337.

Jones, M. B., Marusic, I. & Perry, A. E. 2001 Evolution and structure of sink-flow turbulent boundary layers. *J. Fluid Mech.* **428**, 1.

Keffer, J. F. 1965 The uniform distortion of turbulent wake. *J. Fluid Mech.* **22**, 135.

Moser, R. D., Rogers, M. M. & Ewing, D. W. 1998 Self-similarity of time-evolving plane wakes. *J. Fluid Mech.* **367**, 255.

Narasimha, R. 1989 *Whither turbulence? Turbulence at the crossroads.* In Lecture Notes in Physics, Proceedings of a workshop held at Cornell University, Ithaca New York, March 22–24 (ed. J. Lumley), p. 13, Springer.

Narasimha, R. & Prabhu, A. 1972 Equilibrium and relaxation in turbulent wakes *J. Fluid Mech.* **54**, 1.

Narasimha, R. & Sreenivasan, K. R. 1973 Relaminarization in highly accelerated turbulent boundary layer *J. Fluid Mech.* **61**, 417.

Narasimha, R. & Sreenivasan K. R. 1979 Relaminarisation of fluid flows. *Adv. Appl. Mech.* **19**, 221.

Parsheh, M. 2001 Flow in contractions with application to headboxes. TRITA-PHT Rep. 2000:16 Doctoral thesis, FaxénLaboratoriet, Royal Institute of technology, Stockholm.

Parsheh, M., Brown, M. L. & Aidun, C. K. 2005 On the orientation of stiff fibres suspended in turbulent flow in a planar contraction. *J. Fluid Mech.* **545**, 245.

Pohlhausen, K. 1921 Zur näherungsweisen Integration der Differentialgleichung der laminaren Grenzchicht. *Z. Angew. Math. Mech.* **1**, 252.

Prabhu, A. & Narasimha, R. 1972 Turbulent non-equilibrium wakes. *J. Fluid Mech.* **54**, 19.

Prabhu, A., Narasimha, R. & Sreenivasan, K. R. 1974 Distorted wakes. *Adv. Geophys.* **18B**, 317.

Rogers, M. M. 2002 The evolution of strained turbulent plane wakes. *J. Fluid Mech.* **463**, 53.

Rogers, M. M. 2005 Turbulent plane wakes subjected to successive strains. *J Fluid Mech.* **535**, 215.

Spalart, P. R. 1986 Numerical study of sink flow. *J. Fluid Mech.* **172**, 307.

Sreenivasan, K. R. 1982 Laminariscent, relaminarizing and etransitional flows. *Acta Mech.* **44** 1.

Subsanchandar, N. & Prabhu, A. 1998 Analysis of turbulent near-wake development behind an infinitely yawed flat plate. *Intl J. Non-Linear Mech.* **33**, 1089.

Talamelli, A., Fornaciari, N., Westin, K. J. & Alfredsson, P. H. 2002 Experimental investigation of streaky structures in a relaminarizing boundary layer. *J. Turbul.* **3**, 1.

Townsend, A. A. 1956 *The Structure of Turbulent Shear Flow*. Cambridge University Press.